Journal of the Serbian Chemical Society

Zn(Ta₁₋ₓNbₓ)₂O₆ nanomaterials. Synthesis, characterization and corrosion behaviour

MIHAELA BIRDEANU[1,2]*, GHEORGHE FAGADAR-COSMA[2], IULIANA
SEBARCHIEVICI[1], AUREL-VALENTIN BIRDEANU[3], BOGDAN TARANU[1],
IOAN TARANU[1] and EUGENIA FAGADAR-COSMA[4]

[1]*National Institute for Research and Development in Electrochemistry and Condensed Matter,
1 Plautius Andronescu Street, 300224 Timisoara, Romania,* [2]*Politehnica University of
Timisoara, Vasile Parvan Ave. 6, 300223-Timisoara, Romania,* [3]*National R&D Institute for
Welding and Material Testing – ISIM Timişoara, 20 M. Viteazu Ave., 300222, Timisoara,
Romania and* [4]*Institute of Chemistry Timisoara of the Romanian Academy, 24 M. Viteazu
Ave., 300223-Timisoara, Romania*

Abstract: $Zn(Ta_{1-x}Nb_x)_2O_6$ pseudo-binary oxide nanocrystalline materials
(where $x = 1$, 0.5, 0.1, 0.05 and 0) were obtained through a solid-state method
and characterized by X-ray diffraction (XRD) analysis, Fourier transform infra-
red (FTIR) spectroscopy and ultraviolet–visible (UV–Vis) spectroscopy. In
addition, their morphology and topography were determined by field emission-
-scanning electron microscopy (SEM) and atomic force microscopy (AFM).
There was a significant dependence between the rugosity and the uniformity of
the crystals. Crystals evenly organized in multilayers had the lowest values of
rugosity and non-uniform fractal type architectures had the highest values of
rugosity. The anti-corrosion features of the compounds were evaluated after
deposition on carbon steel (OL) in 0.1 M Na_2SO_4 media by open circuit poten-
tial measurements and the potentiodynamic polarization technique with Tafel
representation. The inhibition efficiency of the pseudo-binary oxides deposited
on a carbon steel electrode was in the range 42.3–52.7 %, which was promising
for their further multiple-layer deposition with porphyrins in order to improve
anticorrosion properties. Due to the high band gap (3.80–4.30 eV), provided by
increasing the tantalum content, four of these pseudo-binary oxides could find
applications in photovoltaic cells.

Keywords: nanomaterials; solid-state method; pseudo-binary oxides; corrosion
inhibition; Tafel curves.

---

* Corresponding author. E-mail: mihaelabirdeanu@gmail.com

INTRODUCTION

Steel,[1] a widely used material in many industries, is prone to corrosion as a result of reactions with the environment. This spontaneous process could compromise the integrity of the material and might cause serious impact on the environment. For these reasons, measures to prevent and control corrosion are required.

Zinc is the most widely used material for protection of steel against corrosion.[2–4] Its corrosion resistance, however, is limited. Zinc alloys can create improved corrosion resistance compared to pure zinc in the protection of ferrous-based metals.[5–9] Efforts to improve the corrosion stability of pure zinc coatings have been directed toward alloying with a more noble metal or adding surface inhibitors.[10] Recently, niobium and tantalate oxides were applied in chemical processing applications due to their outstanding corrosion resistance.[11–13]

Binary niobate and tantalate compounds with the general formula $Zn(Ta_{1-x}Nb_x)_2O_6$ were found to be promising candidates for application in microwave devices based on the improved dielectric properties of these compounds, revealing both a high quality factor ($Q \times f$) and dielelectric constant (ε_r).[14–18]

$ZnTa_2O_6$ was obtained by several modern chemistry preparation routes, *e.g.*, citrate sol–gel,[19] but the most used method is the conventional solid-state reaction of mixed oxides.[17–21] $Zn(Nb_{1-x}Ta_x)_2O_6$ (where $x = 0, 0.2, 0.4, 0.6, 0.8, 0.9$ and 1) novel derivatives exhibiting remarkable dielectric properties were usually prepared by the conventional mixed oxide route.[22]

$ZnNb_2O_6$ was also used as a dielectric[23,24] and was obtained using the molten salt synthesis,[25,26] the sol–gel method,[27] solid-state reaction[23,24,28] and the optical floating zone method.[29] These materials were used in photocatalysis,[30–35] as electrochemical gas sensors,[36] in the energy storage field[37] and in solar cell formulations.[38]

The present study was focused on obtaining three novel pseudo-binary compounds, namely: $Zn(Ta_{1-x}Nb_x)_2O_6$, (where $x = 0.5, 0.1$ and 0.05) and on an investigation regarding their structural, morphological and optical properties in comparison with the already known $ZnNb_2O_6$ and $ZnTa_2O_6$. The effects produced by the increased content of tantalum on the properties of these novel pseudo-binary oxides are discussed. Based on successful experience in corrosion protection (inhibition efficiency up to 96 %) by bilayer depositions of $Zn_3Ta_2O_8$ or $Zn_3Nb_2O_8$ and 5-(4-pyridyl)-10,15,20-tris(4-phenoxy-phenyl)porphyrin or 5-(4-pyridyl)-10,15,20-tris(3,4-dimethoxy-phenyl)porphyrin[39] on carbon steel electrodes, another important aim was to evaluate the anticorrosion activity exhibited by thin films of these compounds on carbon steel in an acid environment.

EXPERIMENTAL

Apparatus. The structural information of the nanomaterials was obtained by X-ray diffraction on an X'pert Pro MPD X-ray diffractometer using CuK_α radiation, at room tempe-

rature. The FTIR measurements were performed on a JASCO 430 FTIR spectrometer in KBr pellets. The morphology and the particle dimensions of the samples were investigated by SEM / EDAX (Model INSPECT S) and AFM (Model Nanosurf® EasyScan 2 Advanced Research). The band gap of the nanomaterials was estimated from the diffuse reflectance spectrum, at room temperature, recorded on an UV–Vis–NIR spectrometer Lambda 950. The electrochemical measurements were realised using a Voltalab potentiostat, Model PGZ 402. The degree of inhibition efficiency, *IE* (%), was calculated based on the equation for the efficiency potential calculation,[40] which is given in the Supplementary material to this paper along with the method for corrosion testing and cell description. The method for corrosion testing and cell description are given in the Supplementary material to this paper.

Reagents. The starting materials used during the synthesis of the $Zn(Ta_{1-x}Nb_x)_2O_6$ (where x = 1, 0.5, 0.1, 0.05 and 0) pseudo-binary oxides were: tantalum(V) oxide (Ta_2O_5, 99.99 %, Sigma), niobium(V) oxide (Nb_2O_5, 99.99 %, Merck) and zinc oxide (ZnO, 99.99 %, Merck).

General method for obtaining $Zn(Ta_{1-x}Nb_x)_2O_6$ (where x = 1, 0.5, 0.1, 0.05 or 0) nanomaterials

$Zn(Ta_{1-x}Nb_x)_2O_6$ (where x = 1, 0.5, 0.1, 0.05 or 0) nanomaterials were obtained by a solid-state method varying the mole ratios (Table I). The obtained materials were in the form of powders and these were subsequently heated at 1200 °C for a soaking time of 3 h. The samples were heated and cooled in a furnace at a rate of 5 °C min⁻¹.

TABLE I. The $Zn(Ta_{1-x}Nb_x)_2O_6$ nanomaterials obtained by a solid-state method

The obtained nanomaterial	x	Mole ratio
$ZnTa_2O_6$	0	ZnO / Ta_2O_5 = 1 / 1
$ZnNb_2O_6$	1	ZnO / Nb_2O_5 = 1 / 1
$Zn(Ta_{0.95}Nb_{0.05})_2O_6$	0.05	$ZnO / Ta_2O_5 / Nb_2O_5$ = 1 / 0.95 / 0.05
$Zn(Ta_{0.9}Nb_{0.1})_2O_6$	0.1	$ZnO / Ta_2O_5 / Nb_2O_5$ = 1 / 0.9 / 0.1
$Zn(Ta_{0.5}Nb_{0.5})_2O_6$	0.5	$ZnO / Ta_2O_5 / Nb_2O_5$ = 1 / 0.5 / 0.5

RESULTS AND DISCUSSION

Structural characterization

The X-ray diffraction patterns for: a) $ZnTa_2O_6$, b) $Zn(Ta_{0.95}Nb_{0.05})_2O_6$, c) $Zn(Ta_{0.9}Nb_{0.1})_2O_6$, d) $Zn(Ta_{0.5}Nb_{0.5})_2O_6$ and e) $ZnNb_2O_6$ are presented in Fig. 1, from which it could be observed that besides the main peaks associated with the $ZnTa_2O_6$ and $ZnNb_2O_6$ pure nanomaterials, some associated peaks appeared (indexed with JCPDS, card No. 01-076-1827 and 01-076-1826), belonging to the *Pbcn* space group.

The intensity of the peaks, relative to the background signal, demonstrates the high purity and good quality of the samples. The highest intensity peak is located at 2θ = 30.4769° for $ZnTa_2O_6$ and 2θ = 30.3424° for $ZnNb_2O_6$, which belong to the 131 plane for $ZnTa_2O_6$ and the 311 plane for $ZnNb_2O_6$.[41] The novel structures have the highest intensity peaks located at 2θ = 30.4569 ° for $Zn(Ta_{0.95}Nb_{0.05})_2O_6$, 2θ = 30.4273° for $Zn(Ta_{0.9}Nb_{0.1})_2O_6$ and 2θ = 30.3964° for $Zn(Ta_{0.5}Nb_{0.5})_2O_6$, the values of which belonging to the interval limited by

$ZnTa_2O_6$ and $ZnNb_2O_6$. A magnified image of the peaks of the XRD pattern in the 2θ range 19–27° is presented in the upper right corner of Fig. 1. As can be observed, at $2\theta = 20.55°$, the intensity of the peak decreased as the Nb concentration increased. The peak situated at $2\theta = 24.67°$ (Fig. 1a), which belong to $ZnTa_2O_6$, is shifted to left with increasing Nb concentration and finally reaches $2\theta = 24.67°$ (Fig. 1e), which corresponds to the $ZnNb_2O_6$ nanomaterial according to JCPDS.
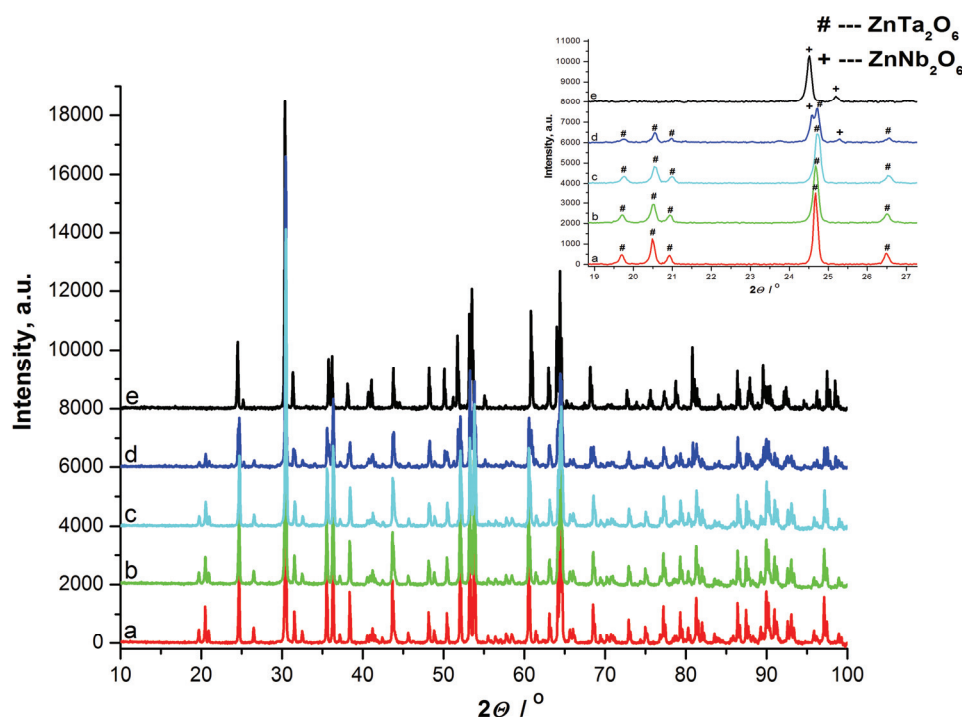
Fig. 1. The XRD patterns of: a) $ZnTa_2O_6$, b) $Zn(Ta_{0.95}Nb_{0.05})_2O_6$, c) $Zn(Ta_{0.9}Nb_{0.1})_2O_6$, d) $Zn(Ta_{0.5}Nb_{0.5})_2O_6$ and e) $ZnNb_2O_6$. Inset: a magnified zone of the XRD patterns containing the peaks for 2θ 19–27°.

The lattice constants were calculated from XRD analysis data, using FullProf Suite computer package:[42] $a = 4.80$ Å, $b = 18.09$ Å, $c = 5.13$ Å, $\alpha = \beta = \gamma = 90°$ and the elementary cell volume ($V / 10^6 / pm^3$) is 409.71 for $ZnTa_2O_6$, while $a = 15.30$ Å, $b = 5.96$ Å, $c = 5.14$ Å, $\alpha = \beta = \gamma = 90°$ and elementary cell volume ($V / 10^6 / pm^3$) is 413.07 for $ZnNb_2O_6$.

The mean crystallite size (d) of the powder samples was calculated using the Scherrer equation.[43] The average crystallite sizes determined from XRD line broadening for each of the samples were: 58 nm for $ZnTa_2O_6$, 47 nm for $Zn(Ta_{0.95}Nb_{0.05})_2O_6$, 42 nm for $Zn(Ta_{0.9}Nb_{0.1})_2O_6$, 39 nm for $Zn(Ta_{0.5}Nb_{0.5})_2O_6$

and 34 nm for $ZnNb_2O_6$. Thus, the values increased with increasing Ta content in the nanomaterial.

The FTIR spectra of the obtained pseudo-binary oxides: a) $ZnNb_2O_6$, b) $ZnTa_2O_6$, c) $Zn(Ta_{0.95}Nb_{0.05})_2O_6$, d) $Zn(Ta_{0.9}Nb_{0.1})_2O_6$ and e) $Zn(Ta_{0.5}Nb_{0.5})_2O_6$ are comparatively presented in Fig. 2.
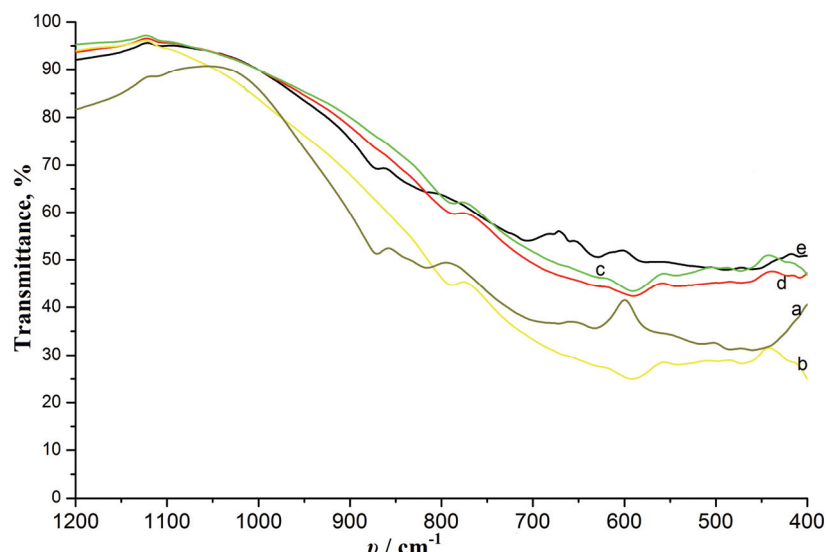
Fig. 2. FTIR spectra of the obtained a) $ZnNb_2O_6$, b) $ZnTa_2O_6$, c) $Zn(Ta_{0.95}Nb_{0.05})_2O_6$, d) $Zn(Ta_{0.9}Nb_{0.1})_2O_6$ and e) $Zn(Ta_{0.5}Nb_{0.5})_2O_6$ materials.

The FTIR spectra of the newly obtained nanomaterials ($Zn(Ta_{1-x}Nb_x)_2O_6$ ($x = 0.5$, 0.1 and 0.05)) displayed some distinctive bands that were located at 600 cm^{-1} for $[Zn(Ta_{0.5}Nb_{0.5})_2O_6]$, 620 cm^{-1} for $[Zn(Ta_{0.9}Nb_{0.1})_2O_6$, $Zn(Ta_{0.95}Nb_{0.05})_2O_6]$ and 640 cm^{-1} for $[Zn(Ta_{0.5}Nb_{0.5})_2O_6]$. Analyzing the structure of the novel nanomaterials and the presence of the known bands from the precursor oxides, these new displayed bands at 640 cm^{-1} and at 620 cm^{-1} could be assigned to Zn–O–Nb and to Zn–O–Ta novel generated bonds. As expected, these new bands were strongly associated with the increased presence of each element in the structure of the nanomaterials. Thus, the intensity of the peaks at 600 cm^{-1} increased with increasing of Ta content, and the position of the peaks tended to be shifted towards lower wave numbers with increasing of ZnO content, in agreement with reported data.[21,44] Moreover, equal mole ratios of Ta and Nb generally favoured large non-resolved bands. Another aspect is that the very weak bands with peaks around 540–560 cm^{-1} could be attributed to symmetrical stretching vibration modes ν_s(O–Metal–O), where the metal is Ta or Nb.

Morphological characterization

　　The morphological aspects of the resulting powders were examined by SEM, as shown in Fig. 3. The micrographs for $ZnNb_2O_6$, $Zn(Ta_{0.5}Nb_{0.5})_2O_6$, $Zn(Ta_{0.9}Nb_{0.1})_2O_6$, $Zn(Ta_{0.95}Nb_{0.05})_2O_6$ and $ZnTa_2O_6$ nanomaterials revealed the formation of soft spherical agglomerates (a) $ZnNb_2O_6$) that display an irregular morphology or fractal-like (e) $ZnTa_2O_6$) crystal structures.
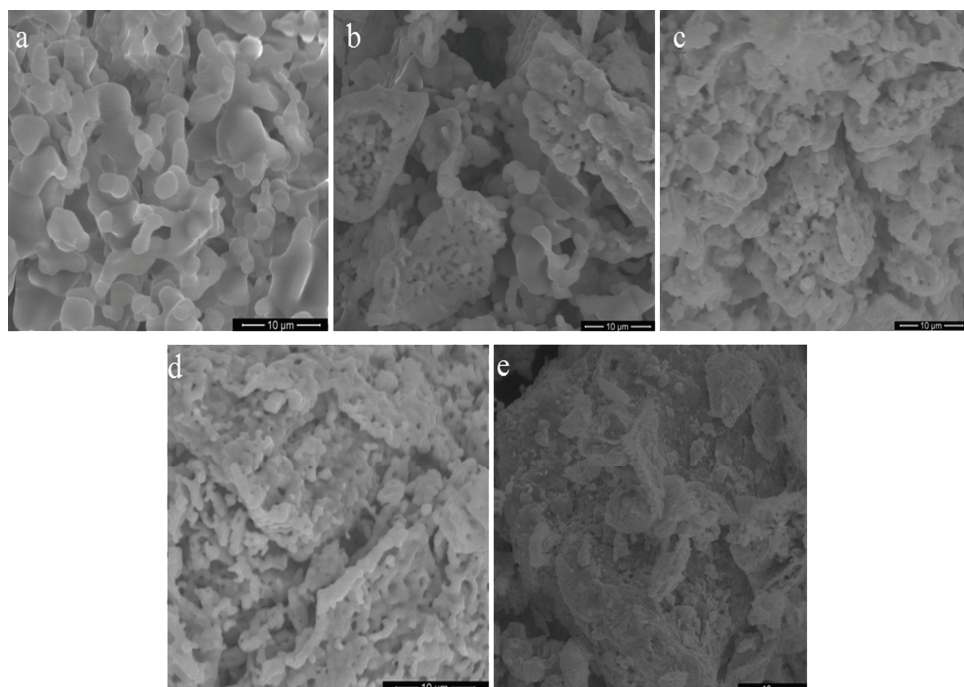

Fig. 3. The SEM images of: a) $ZnNb_2O_6$, b) $Zn(Ta_{0.5}Nb_{0.5})_2O_6$, c) $Zn(Ta_{0.9}Nb_{0.1})_2O_6$, d) $Zn(Ta_{0.95}Nb_{0.05})_2O_6$ and e) $ZnTa_2O_6$.

　　Depending on the nature and chemical composition of the nanomaterials, the morphology was different: crystals organized in multilayer, as in case of $ZnNb_2O_6$, with uniform covering aspect or various size distributed crystals with porous aspect (both mesopores and macropores were present) or even a sponge-like shape in the case of b) $Zn(Ta_{0.5}Nb_{0.5})_2O_6$, c) $Zn(Ta_{0.9}Nb_{0.1})_2O_6$ and d) $Zn(Ta_{0.95}Nb_{0.05})_2O_6$, and a fractal-like aspect in case of e) $ZnTa_2O_6$ (with a touch of an amorphous aspect). The EDAX analysis certified the initial mole ratios between Zn, Nb and Ta, see the Supplementary material for detailed information.

In Figure 4 are shown The AFM images of the surface for each of the studied materials deposited on OL electrodes, using a scan size of 1 μm×1 μm. A contact mode cantilever was used to measure the samples.
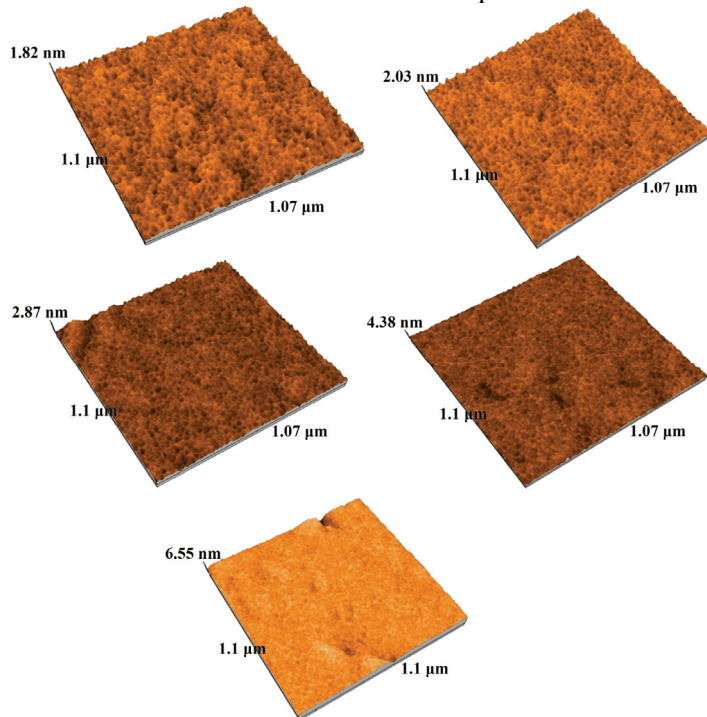
Fig. 4. AFM images of: a) $ZnNb_2O_6$, b) $Zn(Ta_{0.5}Nb_{0.5})_2O_6$, c) $Zn(Ta_{0.9}Nb_{0.1})_2O_6$, d) $Zn(Ta_{0.95}Nb_{0.05})_2O_6$ and e) $ZnTa_2O_6$.

Particle size analysis for $ZnNb_2O_6$, $Zn(Ta_{0.5}Nb_{0.5})_2O_6$, $Zn(Ta_{0.9}Nb_{0.1})_2O_6$, $Zn(Ta_{0.95}Nb_{0.05})_2O_6$ and $ZnTa_2O_6$ deposited on OL electrodes was performed from the AFM measurements data (Nanosurf EasyScan 2 AFM software). The average grain sizes was determined as follows: about 30 nm for $ZnNb_2O_6$, around 38 nm for $Zn(Ta_{0.5}Nb_{0.5})_2O_6$, about 45 nm for $Zn(Ta_{0.9}Nb_{0.1})_2O_6$, about 50 nm for $Zn(Ta_{0.95}Nb_{0.05})_2O_6$ and about 70 nm for $ZnTa_2O_6$, in very good agreement with the results of the XRD measurements. The particle size increased in accordance with the increasing tantalum content. The surface roughness was calculated using equations for the roughness from the literature.[45]

The measured surface had an area of 1.243 pm^2. Using the Nanosurf EasyScan 2 computer software, the values of S_a and S_q for the nanomaterials were calculated as follows: S_a = 0.21 nm and S_q = 0.38 nm for $ZnNb_2O_6$, S_a = = 0.26 nm and Sq = 0.43 nm for $Zn(Ta_{0.5}Nb_{0.5})_2O_6$, S_a = 0.42 nm and S_q = 0.53

nm for $Zn(Ta_{0.9}Nb_{0.1})_2O_6$, $S_a = 0.53$ nm and $S_q = 0.89$ nm for $Zn(Ta_{0.95}Nb_{0.05})_2O_6$ and $S_a = 0.73$ nm and $S_q = 1$ nm for $ZnTa_2O_6$.

There is a strong correlation between the aspect of the samples (SEM images) and the rugosity. The more uniform crystals displayed in multilayers reflect in the lowest value of rugosity and the non-uniform fractal type architectures present the highest value of rugosity. Some failure of the surfaces pro

ducing deep pores and channels could be noticed (Fig. 4c–e).

Optical properties

Using the Kubelka–Munk equation,[46,47] the absorbance was calculated from the reflectance spectra (Fig. 5). The diffuse reflectance spectra were also recorded (Supplementary material to this paper). The plots of $\{(k/s)\ h\nu\}^2$ *vs.* $h\nu$, where k denotes absorption coefficient, s is the scattering coefficient and $h\nu$ is the photon energy, are presented in the inset to Fig. 5. The band gaps were calculated and their values were: 3.20 eV for $ZnNb_2O_6$, 3.80 eV for $Zn(Ta_{0.5}Nb_{0.5})_2O_6$, 4.00 eV for $Zn(Ta_{0.9}Nb_{0.1})_2O_6$, 4.10 eV for $Zn(Ta_{0.95}Nb_{0.05})_2O_6$ and 4.30 eV for $ZnTa_2O_6$. The values of band gap increase in the same manner as the increase the inhibition of corrosion, proving the differentiated chemical stability of the tested nanomaterials.
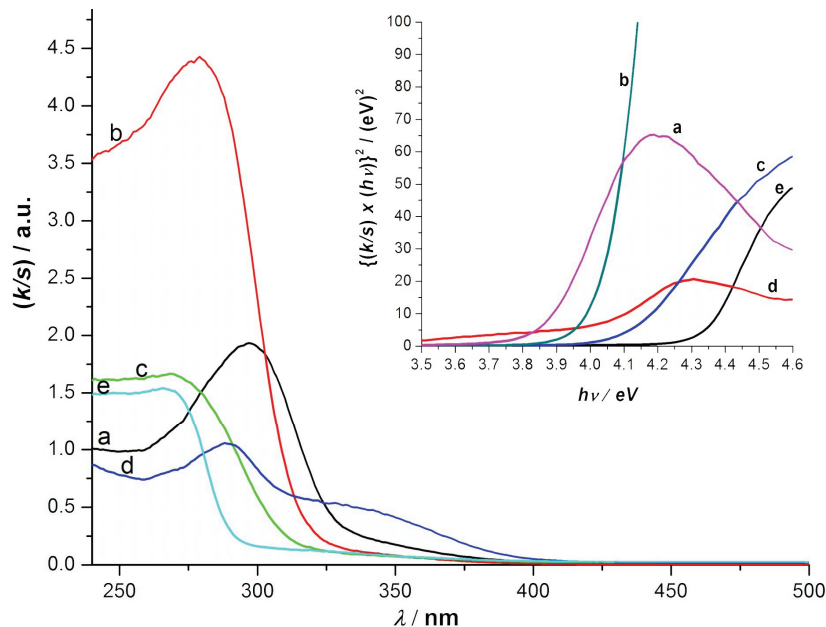

Fig. 5. Absorption spectra of: a) $Zn(Ta_{0.5}Nb_{0.5})_2O_6$, b) $Zn(Ta_{0.9}Nb_{0.1})_2O_6$, c) $Zn(Ta_{0.95}Nb_{0.05})_2O_6$, d) $ZnNb_2O_6$ and e) $ZnTa_2O_6$. Inset: plot of $\{(k/s)h\nu\}^2$ *vs.* $h\nu$ (energy) of: a) $Zn(Ta_{0.5}Nb_{0.5})_2O_6$, b) $Zn(Ta_{0.9}Nb_{0.1})_2O_6$, c) $Zn(Ta_{0.95}Nb_{0.05})_2O_6$, d) $ZnNb_2O_6$ and e) $ZnTa_2O_6$.

Tafel plots

Tafel plots of the investigated OL electrodes, recorded after 30 min OCP (Supplementary material) in 0.1 M Na_2SO_4 solution, are shown in Fig. 6. The parameters calculated from these plots are summarized in Table II.
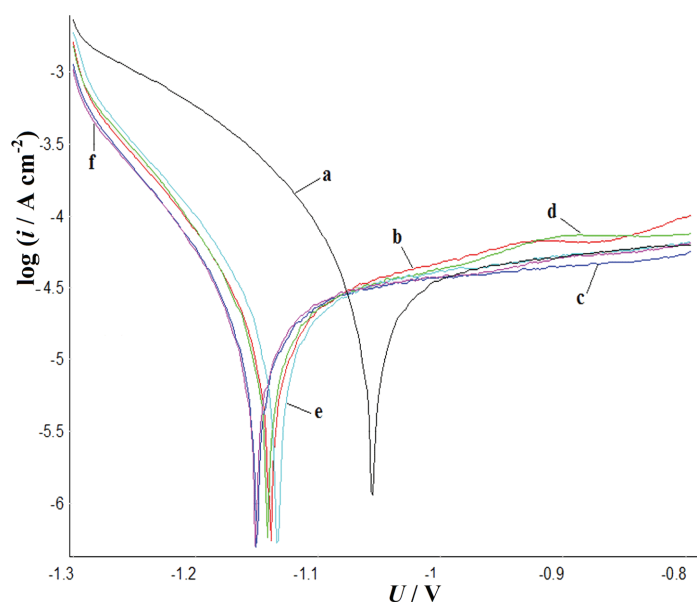

Fig. 6. Tafel representation of polarization curves recorded in 0.1 M Na_2SO_4 for the studied electrodes. a) OL, b) $ZnTa_2O_6$, c) $ZnNb_2O_6$, d) $Zn(Ta_{0.95}Nb_{0.05})_2O_6$, e) $Zn(Ta_{0.9}Nb_{0.1})_2O_6$ and f) $Zn(Ta_{0.5}Nb_{0.5})_2O_6$.

The slopes were determined in the Tafel region of the anodic and cathodic curves for segments of approximately 50 mV.

The current density corresponds to the rate of the electrochemical reactions associated with corrosion processes taking place on the OL surface, under polarization in 0.1 M Na_2SO_4 media.

TABLE II. Tafel parameters of the investigated electrodes after 30 min immersion in 0.1 M Na_2SO_4 solution

Electrode	E_{corr} / V	i_{corr} / µA cm^{-2}	Rp / kΩ cm^2	v_{corr} / µm y^{-1}	IE / %
Bare OL	−1.05	40.36	0.90	469.1	–
$ZnTa_2O_6$	−1.14	20.74	1.40	241.1	48.61
$ZnNb_2O_6$	−1.15	19.09	1.41	221.9	52.70
$Zn(Ta_{0.95}Nb_{0.05})_2O_6$	−1.14	23.25	1.34	270.2	42.39
$Zn(Ta_{0.9}Nb_{0.1})_2O_6$	−1.13	22.51	1.27	261.7	44.22
$Zn(Ta_{0.5}Nb_{0.5})_2O_6$	−1.15	21.23	1.43	246.8	47.40

The corrosion potential (E_{corr}) of the bare OL electrode was -1.05 V and the corresponding corrosion current density (i_{corr}) was 40.36 μA cm^{-2}. In all cases the presence of $Zn(Ta_{1-x}Nb_x)_2O_6$ shifted the polarization curves towards the region of lower corrosion current densities because of the better stability of the covering metal oxides. For all the studied covering materials, a similar corrosion inhibiting activity was observed, as presented in Table II. The differences in the inhibition efficiencies (*IE*) were probably generated by the differences in the stability of these materials, the roughness and the porosity of the protective coatings. Comparing, for instance, $ZnNb_2O_6$ and $ZnTa_2O_6$, the average roughness increased from $S_a = 0.21$ nm to $S_a = 0.73$ nm and the *IE* decreased from 52.7 to 48.61 %, respectively. Furthermore, $ZnNb_2O_6$ had a uniform covering aspect being less porous than $ZnTa_2O_6$. This study clearly showed that a decrease in the niobium content in the pseudo-binary oxides was accompanied by an increase in the average roughness values, which had the effect of decreasing the inhibition efficiency.

The shift of E_{corr} towards negative values in the presence of $Zn(Ta_{1-x}Nb_x)_2O_6$ was caused by the different nature of the electrochemically active species from the metal surface (Zn, Ta and Nb) besides Fe. The presence of solely niobium ions next to the zinc ones (the case of $ZnNb_2O_6$) shifted the corrosion potential towards more negative values (-1.15 V), the corrosion current density being decreased from 40.36 (OL) to 19.09 μA cm^{-2}, which means a decrease in the corrosion rate (v_{corr}) and a better inhibition efficiency.

The polarization resistance (R_p) increased slightly from 0.9 for bare OL to 1.43 kΩ cm^2 for the $Zn(Ta_{0.5}Nb_{0.5})_2O_6$ covered electrode, also indicating an inhibition of the corrosion in the presence of $Zn(Ta_{1-x}Nb_x)_2O_6$ nanomaterials.

CONCLUSIONS

Three novel pseudo-binary oxides, namely: $Zn(Ta_{0.5}Nb_{0.5})_2O_6$, $Zn(Ta_{0.9}Nb_{0.1})_2O_6$ and $Zn(Ta_{0.95}Nb_{0.05})2O_6$ were obtained by a solid-state method and comparatively characterized by XRD, FTIR, SEM/EDAX, AFM and UV–Vis investigations with the already known $ZnNb_2O_6$ and $ZnTa_2O_6$ compounds.

The existence of a single crystalline phase and the average crystallite size were evidenced from the XRD diagrams and confirmed by the AFM measurements. A strong correlation between the aspect of the samples (SEM images) and the rugosity properties was found. The nanomaterial capacity to agglomerate might justify the continuous and uniform covering of the OL materials.

The structure of the studied materials was confirmed by FTIR spectroscopy and EDAX analysis. The values of the band gap increased in the order: $ZnNb_2O_6$, $Zn(Ta_{0.5}Nb_{0.5})_2O_6$, $Zn(Ta_{0.9}Nb_{0.1})_2O_6$, $Zn(Ta_{0.95}Nb_{0.05})_2O_6$ and $ZnTa_2O_6$, which followed the increased chemical stability of the tested material with inc-

reasing tantalum content, recommending these materials for application in photo-voltaic cells.

The electrochemical parameters of the Tafel plots illustrate corrosion inhibition in the presence of all the new synthesized $Zn(Ta_{1-x}Nb_x)_2O_6$ compounds deposited on an OL surface. The combinations of Zn oxide with Ta and Nb oxides evidently increased the inhibition efficiency with increasing niobium content in the material. The best results revealed that a $ZnNb_2O_6$ treated electrode exhibited an inhibition efficiency of 52.7 %.

Due to the inhibition efficiency of pseudo-binary oxides deposited on carbon steel electrode, the nanomaterials with increased niobium content will be used in multiple layer deposition with porphyrins in order to improve anticorrosion properties. Due to the high band gaps (3.80–4.30 eV) provided by increasing the tantalum content, four of these pseudo-binary oxides might find applications in photovoltaic cells.

SUPPLEMENTARY MATERIAL

Additional experimental details, the results of EDAX and optical analyses and the open circuit potential measurements are available electronically from http://www.shd.org.rs/JSCS/, or from the corresponding author on request.

ИЗВОД

Zn(Ta$_{1-x}$Nb$_x$)$_2$O$_6$ НАНОМАТЕРИЈАЛИ. СИНТЕЗА, КАРАКТЕРИЗАЦИЈА И КОРОЗИОНО ПОНАШАЊЕ

MIHAELA BIRDEANU[1,2], GHEORGHE FAGADAR-COSMA[2], IULIANA SEBARCHIEVICI[1], AUREL-VALENTIN BIRDEANU[3], BOGDAN TARANU[1], IOAN TARANU[1] и EUGENIA FAGADAR-COSMA[4]

[1]*National Institute for Research and Development in Electrochemistry and Condensed Matter, 1 Plautius Andronescu Street, 300224 Timisoara, Romania,* [2]*Politehnica University of Timisoara, Vasile Parvan Ave.6, 300223-Timisoara, Romania,* [3]*National R&D Institute for Welding and Material Testing - ISIM Timişoara, 20 M. Viteazu Ave., 300222, Timisoara, Romania и* [4]*Institute of Chemistry Timisoara of Romanian Academy, 24 M. Viteazu Ave, 300223-Timisoara, Romania*

Помоћу методе чврсто стање добијени су псеудо-бинарни оксиди опште формуле Zn(Ta$_{1-x}$Nb$_x$)$_2$O$_6$ (где је x = 1; 0,5; 0,1; 0,05 и 0). Ови нанокристални материјали су окарактерисани помоћу методе дифракције X-зрака и Фуријеове трансформационе инфрацрвене и UV−Vis спектроскопије. Морфологија и топографија ових нанокристал-них материјала је одређена помоћу емисионе скенирајуће електронске микроскопије (SEM) и атомске микроскопије поља (AFM). Нађена је значајна зависност између набо-раности и униформности кристала. Равномерно слојевито организовани кристали имају најнижу вредност набораности, док кристали неравномерне фракталне структуре имају

највеће вредности набораности. Антикорозионе особине једињења су испитиване након депозиције на угљенични челик (OL) у 0,1 M Na_2SO_4 помоћу мерења потенцијала отвореног кола и потенциодинамичке поларизационе технике преко Тафелових зависности. Ефикасност инхибиције таложења псеудо-бинарних оксида на електроди од угљеничног челика била је у опсегу 42,3–52,7 %, што може имати утицаја на њихову слојевиту депозицију у присуству порфирина, као и боља антикорозиона својства. С обзиром на чињеницу да долази до великог скока потенцијала (3,80–4,30 eV) приликом повећања садржаја тантала, може се претпоставити да четири испитивана псеудо-би-нарна оксида могу потенцијално имати примену у фотонапонским ћелијама.

REFERENCES

1. B. H. Ali, B. S. Ali, R. Yusoff, M. K. Aroua, *J. Electrochem. Sci.* **6** (2011) 181
2. M. Zemanova, *Chem. Pap.* **63** (2009) 574
3. S. Yogesha, A. C. Hegde, *Trans. Indian Inst. Met.* **63** (2010) 841
4. R. N. Jagtap, P. P. Patil, S. Z. Hassan, *Prog. Org. Coat.* **63** (2008) 389
5. A. P. Patil, R. H. Tupkary, *Trans. Indian Inst. Met.* **62** (2009) 71
6. A. Roshanghias, M. Heydarzadeh Sohi, *J. Coat. Technol. Res.* **9** (2012) 215
7. H. Shi, F. Liu, E. Han, Y. Wei, *J. Mater. Sci. Technol.* **23** (2007) 551
8. Q. An, Y. Xin, K. Huo, X. Cai, P. K. Chu, *Mater. Chem. Phys.* **115** (2009) 439
9. A. P. I. Popoola, O. S. I. Fayomi, *Int. J. Phys. Sci.* **6** (2011) 2447
10. A. E. Elsherief, M. A. Shoeb, *Corr. Prev. Control* **50** (2003) 25
11. R. A. Grahan, R. C. Sutherlin, in *Proceedings of the International Symposium Niobium 2001*, Orlando, FL, USA, 2001, p. 337
12. J.-P. Masse, H. Szymanowski, O. Zabeida, A. Amassian, J. E. Klemberg-Sapieha, L. Martinu, *Thin Solid Films* **515** (2006) 1674
13. K. Kamada, M. Mukai, Y. Matsumoto, *Electrochim. Acta* **49** (2004) 321
14. J.-H. Park, S. Nahm, J.-G. Park, *J. Alloys Compd.* **537** (2012) 221
15. Y. C. Zhang, B. Fu, X. Wang, *J. Alloys Compd.* **478** (2009) 498
16. S. Wu, J. Luo, *J. Alloys Compd.* **509** (2011) 8126
17. W.-S. Xia, G.-Y. Zhang, L.-W. Shi, M.-M. Zhang, *Mater. Lett.* **124** (2014) 64
18. B. Fu, Y. Zhang, H. Yue, *Ceram. Int.* **39** (2013) 3789
19. Y. C. Zhang, B. J. Fu, X. Wang, *J. Alloys Compd.* **478** (2009) 498
20. Y. NuLi, Z.-W. Fu, Y.-Q. Chu, Q.-Z. Qin*, Solid State Ionics* **160** (2003) 197
21. M. Bîrdeanu, A.-V. Bîrdeanu, E. Fagadar-Cosma, C. Enache, I. Miron, I. Grozescu, *Dig. J. Nanomater. Biosci.* **8** (2013) 263
22. Y. C. Zhang, Z. X. Yue, X. Qi, B. Li, Z. L. Gui, L. T. Li, *Mater. Lett.* **58** (2004) 1392
23. H. B. Bafrooei, E. T. Nassaj, T. Ebadzadeh, C. Hu, *Ceram. Int.* **40** (2014) 14463
24. G. Feng, L. Jiaji, H. Rongzi, L. Zhen, T. Changsheng, *Ceram. Int.* **35** (2009) 2687
25. L. Guo, J. Dai, J. Tian, Z. Zhu, T. He, *Mater. Res. Bull.* **42** (2007) 2013
26. L. Guo, J. Dai, J. Tian, T. He, *Ceram. Int.* **34** (2008) 1783
27. C.-H. Hsu, P.-C. Yang, H.-W. Yang, S.-F. Yan, H.-H. Tung, *Thin Solid Films* **519** (2011) 5030
28. L. B. Kong, J. Ma, H. Huang, R. F. Zhang, T. S. Zhang, *J. Alloys Compd.* **347** (2002) 308
29. D. Xu, Y. Liu, Q. Zhou, T. Cui, H. Yuan, W. Wang, Z Shi, L. Li, *J. Alloys Compd.* **618** (2015) 694
30. W. Wu, S. Liang, Z. Ding, H. Zheng, L. Wu, *Solid State Sci.* **13** (2011) 2019
31. L. Zhang, I. Djerdj, M. Cao, M. Antonietti, M. Niederberger, *Adv. Mater.* **19** (2007) 2083

32. Z. Ding, W. Wu, S. Liang, H. Zheng, L. Wu, *Mater. Lett*. **65** (2011) 1598
33. S. Liang, L. Wu, J. Bi, W. Wang, J. Gao, Z. Li, X. Fu, *Chem. Commun*. **46** (2010) 1446
34. D. Chen, J. Ye, *Chem. Mater*. **21** (2009) 2327
35. K. Saito, A. Kudo, *Inorg. Chem*. **49** (2010) 2017
36. S. A. Anggraini, M. Breedonb, N. Miura, *Sens. Actuators B* **187** (2013) 58
37. T. Wang, X. Wei, Q. Hu, L. Jin, Z. Xu, Y. Feng, *Mater. Sci. Eng. B* **178** (2013) 1081
38. Y.-J. Hsiao, T.-H. Fang, L.-W. Ji, *Mater. Lett.* **64** (2010) 2563
39. M. Birdeanu, A.-V. Birdeanu, I. Popa, B. Taranu, F. Peter, I. Creanga, A. Palade, E. Fagadar-Cosma, in *Proceedings of NANOCON 2014 Conference*, Ostrava, Czech Republic, Tanger, 2015, p. 262
40. Z. Ahmad, *Principles of Corrosion Engineering and Corrosion Control*, Butterworth-Heinemann/IChemE Series, Elsevier, Amsterdam, 2006, p. 377
41. S. K. Kurinec, P. D. Rack, M. D. Potter, T. N. Blanton, *J. Mater. Res*., **15** (2000) 1320
42. www.ill.eu/sites/fullprof/
43. T. Minami, H. Sato, K. Ohashi, T. Tomofuji, S. Takata, *J. Cryst. Growth* **117** (1992) 370
44. M. Bîrdeanu, A.-V. Bîrdeanu, A. S. Gruia, E. Fagadar-Cosma, C. N. Avram, *J Alloys Compd*. **573** (2013) 53
45. V. Kapaklis, P. Poulopoulos, V. Karoutsos, Th. Manouras, C. Politis, *Thin Solid Films* **510** (2006) 138
46. P. Kubelka, F. Munk, *Zh. Tekh. Fiz*. **12** (1931) 593
47. P. Kubelka, *J. Opt. Soc. Am.* **38** (1948) 448.